

Robust Image Stitching with Optimal Plane

Lang Nie^{1,*}, Yuan Mei^{2,*}, Kang Liao³, Yunqiu Xu⁴, Chunyu Lin⁵, Bin Xiao¹

¹Chongqing Key Laboratory of Image Cognition, Chongqing University of Posts and Telecommunications,

²The Hong Kong Polytechnic University, ³Nanyang Technological University,

⁴Zhejiang University, ⁵Beijing Jiaotong University

nielang@cqupt.edu.cn, yyuan.mei@connect.polyu.hk, kang.liao@ntu.edu.sg,

imyunquixu@gmail.com, cylin@bjtu.edu.cn, xiaobin@cqupt.edu.cn

Abstract

We present *RopStitch*, an unsupervised deep image stitching framework with both robustness and naturalness. To ensure the robustness of *RopStitch*, we propose to incorporate the universal prior of content perception into the image stitching model by a dual-branch architecture. It separately captures coarse and fine features and integrates them to achieve highly generalizable performance across diverse unseen real-world scenes. Concretely, the dual-branch model consists of a pretrained branch to capture semantically invariant representations and a learnable branch to extract fine-grained discriminative features, which are then merged into a whole by a controllable factor at the correlation level. Besides, considering that content alignment and structural preservation are often contradictory to each other, we propose a concept of virtual optimal planes to relieve this conflict. To this end, we model this problem as a process of estimating homography decomposition coefficients, and design an iterative coefficient predictor and minimal semantic distortion constraint to identify the optimal plane. This scheme is finally incorporated into *RopStitch* by warping both views onto the optimal plane bidirectionally. Extensive experiments across various datasets demonstrate that *RopStitch* significantly outperforms existing methods, particularly in scene robustness and content naturalness. The code is available at <https://github.com/MmelodyYy/RopStitch>.

1 Introduction

Image stitching, a long-standing task (Brown and Lowe 2007) in computer vision, aims to generate a wide FoV panorama from multiple images with limited FoV, while minimizing content artifacts and shape distortions. Besides enabling user creation and entertainment, it has been widely applied in various fields such as virtual reality, autonomous driving, and intelligent surveillance.

Traditional image stitching algorithms have achieved considerable success in both content alignment (Zaragoza et al. 2013) and shape preservation (Chen and Chuang 2016), but they typically rely on an implicit assumption, *i.e.*, the presence of texture-rich scenes with distinct features. When this assumption is not satisfied, these traditional algorithms can cause performance degradation or even failure, especially in low-texture or low-light scenes, where hand-crafted features

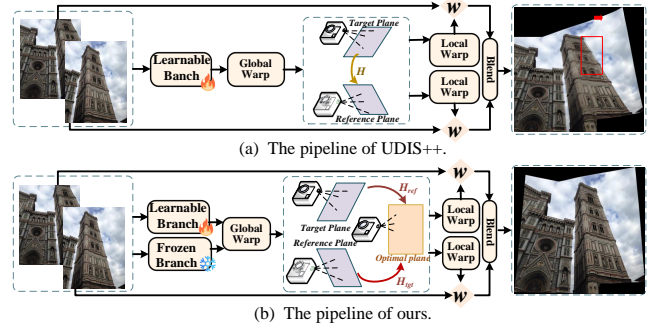


Figure 1: Difference from existing solutions. (a) UDIS++ (Nie et al. 2023) uses a single-branch architecture and a single reference plane, resulting in limited cross-scene generalization and content stretching. (b) Our method incorporates perceptual prior through a dual-branch architecture and aligns images on a virtual optimal plane, thereby enhancing cross-scene generalization and natural appearance.

(*e.g.*, keypoint (Lowe 2004), line segment (Von Gioi et al. 2008), etc.) are not sufficiently and evenly detected.

In contrast, deep image stitching solutions get rid of this limitation by digging into high-level semantic features (Nie et al. 2021b) instead of shallow geometric cues, whose capability is acquired through fitting abundant data to enable general semantic perception. However, limited by the scale of existing image stitching datasets (*e.g.*, UDIS-D (Nie et al. 2021b) only contains about 10k samples), the pre-trained models struggle to achieve highly generalizable performance across diverse unseen real-world scenarios due to the domain distribution gap between different datasets.

To overcome the above issues, as shown in Fig. 1, we propose to incorporate the universal prior (acquired by large-scale datasets) into the image stitching model (trained on limited data quantity). To this end, we present a robust image stitching model with a dual-branch architecture. The first branch leverages a pretrained backbone from large-scale datasets (Deng et al. 2009) to capture semantically invariant features, which implicitly contain the prior of coarse but robust content perception. The other branch adopts a learnable backbone to extract fine-grained discriminative features, which serves as a perfect complement to provide fine

*The first two authors contribute equally.

but dedicated semantics. To combine the advantages of different branches, we carry out the feature aggregation process in the correlation layer, which first calculates respective correlation volumes and then merges them by a controllable factor. The merged correlation is used to predict stable warping parameters and realize robust image stitching.

Furthermore, we propose to relieve the conflict between content alignment and shape preservation by identifying an optimal stitching plane. It decreases the distortion by redistributing the warping burdens from a single view to different views according to a principle of minimal semantic distortions. Specifically, we reformulate the process of determining the optimal plane as generating a set of coefficients for homography decomposition. To find the desired coefficients, we design an iterative coefficient predictor to disentangle a given homography matrix into two and a corresponding semantic distortion constraint to comprehensively measure the deformation distortion and semantic significance. The stitching naturalness can be increased through projecting different views onto the optimal plane bidirectionally.

With the proposed dual-branch architecture and optimal plane, we construct a new unsupervised image stitching framework, named *RopStitch*, which demonstrates superior performance, especially in robustness and naturalness. Our main contributions are centered around:

- To improve robustness in real-world scenes, we propose to integrate the universal prior into the image stitching model through a dual-branch architecture.
- To decrease structure distortions, we present to determine an optimal stitching plane at the principle of minimal semantic distortions without sacrificing content alignment.
- The proposed framework, *RopStitch*, outperforms existing solutions, particularly in scene robustness and content naturalness.

2 Related work

2.1 Traditional Image Stitching

Traditional solutions typically leverage hand-crafted features to estimate the desired warps. According to the optimization objectives, these methods can be divided into two categories: (1) alignment-oriented approaches, and (2) structure-preserving approaches. For the first category, existing researches adopt the homography (Brown and Lowe 2007), mesh (Zaragoza et al. 2013), TPS (Li et al. 2017), triangular facet (Li et al. 2019; Cai and Yang 2025), and even subpixel (Lee and Sim 2020) to achieve increasingly flexible transformations. To assist this process, some works further use semantic segmentation (Li, Guo, and Guo 2021; Liao et al. 2025) or depth maps (Liao and Li 2022) to filter non-planar outliers. But excessive alignment often leads to structural distortion, especially in large parallax areas. For the other category, existing methods adopt diverse geometric features beyond keypoints, including line segment (Von Gioi et al. 2008), edge (Du et al. 2022), and even object segmentation (Cai and Yang 2025) to estimate or optimize a structure-preserving warp (Liao and Li 2019; Jia et al. 2021; Chen and Chuang 2016; Lin et al. 2015; Li et al. 2024). But

this kind of warp will lose its preservation capability when the scenes lack these specific features. Also, better structure naturalness inevitably sacrifices alignment accuracy to a certain extent and tends to produce artifacts.

Although these methods have demonstrated promising performance, their reliance on hand-crafted features inherently limits robustness to scenarios with sufficient feature availability.

2.2 Deep Image Stitching

Compared with traditional approaches, deep image stitching methods exhibit inherent robustness advantages, owing to CNNs’ capability to extract high-level semantic features. These methods also follow a similar development trend to traditional approaches, such as homography-based (Mei et al. 2024; Jiang et al. 2022; Ma et al. 2023), mesh-based (Nie et al. 2023, 2025; Zhang et al. 2024), and pixel-based (Jia et al. 2023; Kweon et al. 2023) solutions. These solutions input an image pair into the neural networks and directly output the warping parameters, totally discarding traditional hand-crafted features. Besides, to enhance cross-domain generalization capability, deep stitching solutions are undergoing an evolution from supervised (Nie et al. 2020, 2022; Dai et al. 2021; Edstedt et al. 2024) to weakly-supervised (Song et al. 2022), and ultimately to unsupervised learning (Nie et al. 2021b, 2023, 2025; Jia et al. 2023; Jiang et al. 2022, 2024) paradigms.

However, even the most robust unsupervised methods inevitably face domain gap challenges between training and real-world data. This persistent generalization issue remains the most pressing challenge for unsupervised approaches.

3 Methodology

3.1 Overview

RopStitch employs a global-to-local warping strategy, which is similar to UDIS++ (Nie et al. 2023). In the global stage, we estimate the homography as the global transformation, while in the local stage, we adopt mesh deformation specified by TPS control points (Bookstein 1989). The main difference lies in two aspects: dual-branch architecture and virtual optimal plane. As shown in Fig. 2(top), given a pair of reference and target images (I_{ref} and I_{tgt}), the dual-branch architecture outputs a global homography H , which contains an implicit universal prior and enables robust estimation. Then H is decomposed into H_{ref} and H_{tgt} to identify the optimal plane. Subsequently, the local stage predicts respective TPS transformations, carrying out bidirectional elastic warping on the desired plane.

As for the objective function, it consists of three terms as follows:

$$\mathcal{L} = \mathcal{L}_{align} + \mathcal{L}_{shape} + \mathcal{L}_{coef}, \quad (1)$$

where \mathcal{L}_{align} and \mathcal{L}_{shape} constrain the content alignment and shape preservation, which are similar to UDIS++, and we would discuss them in the supplementary materials. \mathcal{L}_{coef} is the constraint to determine an optimal plane, which is described in detail in Sec. 3.3.

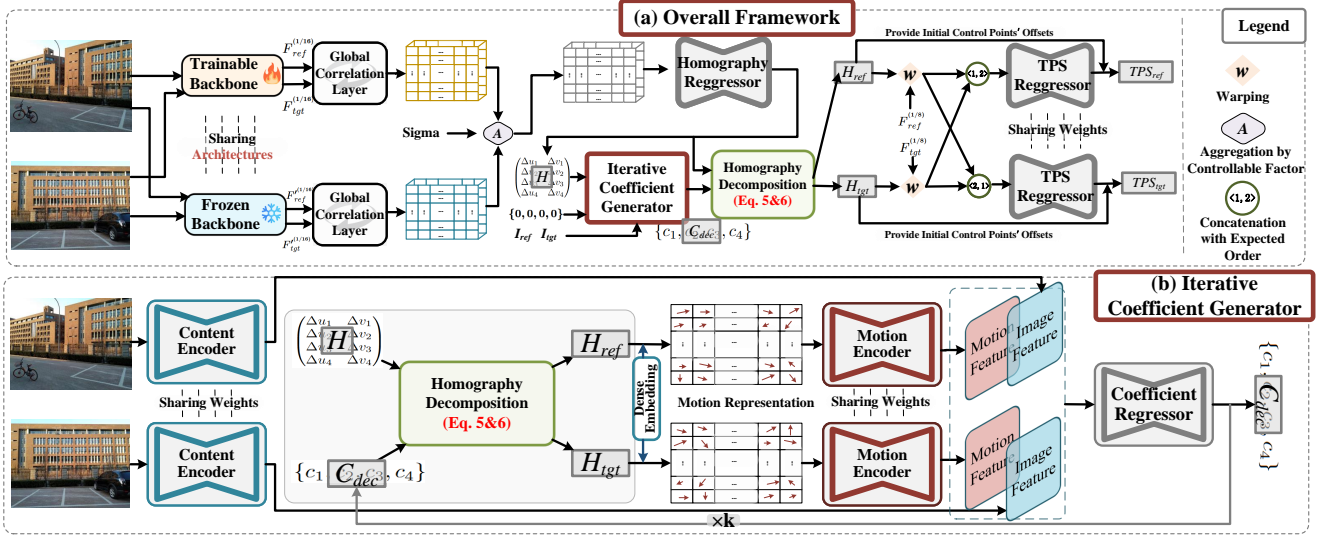


Figure 2: The framework of *RopStitch*. It takes a dual-branch architecture to construct a robust correlation volume, thereby ensuring robust global transformation. Then the single-view projection is decomposed into two bidirectional warps on the optimal plane, which is followed by the bidirectional local deformation.

3.2 Dual-branch Architecture

Generalizing across diverse scenes is a major bottleneck for stitching algorithms. Fortunately, large-scale pre-trained models often inherently possess the capability of cross-scene understanding. To leverage such universal priors, we constructed a dual-branch architecture designed to separately represent learnable features and invariant features from the raw input images. Specifically, we built a Siamese backbone network that was pre-trained on the ImageNet dataset. These two backbones ($f_{frozen}(\cdot)$ and $f_{train}(\cdot)$) share an identical network structure; the sole distinction is that one backbone remains entirely frozen throughout the training process, while the other is kept active (trainable). Furthermore, a potential advantage of the Siamese network structure is its capacity to effectively alleviate discrepancies in feature representations between the two streams, which positively advances the subsequent motion regression and facilitates the cross-domain robustness, as validated in Table 3.

Concretely, we leverage $f_{frozen}(\cdot)$ and $f_{train}(\cdot)$ to extract the 1/8 and 1/16 scale variable features for an input pair (I_{ref} and I_{tgt}), respectively. The specific formula is as follows:

$$\begin{aligned} F_{ref}^{(1/8)}, F_{ref}^{(1/16)}; F_{tgt}^{(1/8)}, F_{tgt}^{(1/16)} &= f_{train}(I_{ref}; I_{tgt}), \\ F_{ref}'^{(1/16)}; F_{tgt}'^{(1/16)} &= f_{frozen}(I_{ref}; I_{tgt}). \end{aligned} \quad (2)$$

Correlation-wise Aggregation With the introduction of a frozen backbone, we are able to extract invariant feature representations from the input images. However, the optimal usage of these invariant features remains an open research question. The most straightforward approach is to directly add or concatenate the features. However, such methods often lead to convergence between the learnable and invariant

features, resulting in redundant feature representations. Similarly, dynamic feature fusion strategies may cause the fusion mechanism to become overly dependent on the training dataset, thereby limiting the model’s generalization ability in cross-domain scenarios.

To address these challenges, we propose to shift the fusion process to the correlation level. After computing the global correlation using CCL (Nie et al. 2021a), the resulting volumes ($Corr_{train}, Corr_{frozen} \in \mathbb{R}^{2 \times \frac{H}{16} \times \frac{W}{16}}$) effectively capture the dense spatial correspondences between the reference and target images. The specific formula is as follows:

$$\begin{aligned} Corr_{train} &= CCL(F_{ref}^{(1/16)}, F_{tgt}^{(1/16)}), \\ Corr_{frozen} &= CCL(F_{ref}'^{(1/16)}, F_{tgt}'^{(1/16)}). \end{aligned} \quad (3)$$

Subsequently, by performing aggregation at the level of the global correlation map, we can circumvent the aforementioned issues and achieve more effective integration of invariant features and learnable features. However, how to fuse these features in a manner that simultaneously enhances the robustness of the learnable backbone and preserves the representational stability of the frozen backbone remains a problem to be solved. Inspired by the Variational Autoencoder (VAE) framework (Kingma, Welling et al. 2013), we employ a **random** sigma value ($\sigma \in \mathbb{R}^{2 \times 1 \times 1}$) within the range $[0, 1]$ during training to fuse the features, analogous to the roles of variance and mean in VAEs. The introduction of random σ extends the model’s capacity to represent global correlation maps of varying strengths, rather than being restricted to the optimal correlation patterns present in the training data. This process can be written as:

$$Corr_{fusion} = (1 - \sigma) \cdot Corr_{train} + \sigma \cdot Corr_{frozen}. \quad (4)$$

To fully exploit the prior knowledge encoded in the frozen backbone, we employ a ternary search strategy during inference to adaptively adjust σ within the range of $[-1, 2]$. Doubling the search outwards is equivalent to performing a complementary operation of residual relevance. These approaches significantly enhances the model’s cross-domain stitching performance, as demonstrated in Table 4 and the supplementary material.

Finally, the $Corr_{fusion}$ is fed into a subsequent global regression network to predict the four-point offsets. The global homography matrix H is then obtained using the method described in (Cai et al. 2025).

3.3 Warping on Optimal Plane

Existing image stitching methods typically warp one image to align with the other. But this strategy places the entire warping burden on a single view, easily yielding excessive deformation and projective distortions. To this end, we propose the concept of optimal stitching planes and carry out bidirectional warping.

Concretely, we use homography H to represent the plane and decompose this transformation into two (H_{ref} , H_{tgt}) to denote the warps from respective planes to the optimal plane. Denoting H with 4-pt representation (DeTone, Malisiewicz, and Rabinovich 2016), we can define H_{tgt} with decomposition coefficients $C_{dec} = \{c_1, c_2, c_3, c_4\}$, in which $c_i \in [0, 1]$ corresponds to one of the four vertexes. This process can be written as:

$$H \sim \begin{pmatrix} \Delta u_1 & \Delta v_1 \\ \Delta u_2 & \Delta v_2 \\ \Delta u_3 & \Delta v_3 \\ \Delta u_4 & \Delta v_4 \end{pmatrix}, H_{tgt} \sim \begin{pmatrix} \Delta c_1 u_1 & \Delta c_1 v_1 \\ \Delta c_2 u_2 & \Delta c_2 v_2 \\ \Delta c_3 u_3 & \Delta c_3 v_3 \\ \Delta c_4 u_4 & \Delta c_4 v_4 \end{pmatrix}, \quad (5)$$

where $(\Delta u_i, \Delta v_i)$ are the offsets of i -th vertex. Then we can derive H_{ref} as follows:

$$H_{ref} = H^{-1} H_{tgt}. \quad (6)$$

Apparently, the key to determining the optimal plane is to precisely identify the decomposition coefficients. To this end, we design an iterative coefficient generator and the corresponding objective function to ensure minimal semantic distortion.

Iterative Coefficient Generator As illustrated in Fig. 2(bottom), the iterative coefficient generator consists of three sub-networks: content encoder, motion encoder, and coefficient regressor. The content encoder takes two views as input and encodes them into latent image features, while the motion encoder inputs dense motion representations and encodes them into latent motion features. Given a 3×3 homography matrix $H = (h_1, h_2, h_3)^T$ (where $h_i \in \mathbb{R}^{3 \times 1}$), we can embed it into pixel-wise motion representation as:

$$m_{x,y} = \begin{pmatrix} h_1 \cdot (x \ y \ 1)^T \\ h_2 \cdot (x \ y \ 1)^T \\ h_3 \cdot (x \ y \ 1)^T \end{pmatrix} - \begin{pmatrix} x \\ y \end{pmatrix}, \quad (7)$$

where (x, y) denotes the pixel location in an image. After acquiring the image and motion features, a coefficient regressor is leveraged to aggregate these features and generate

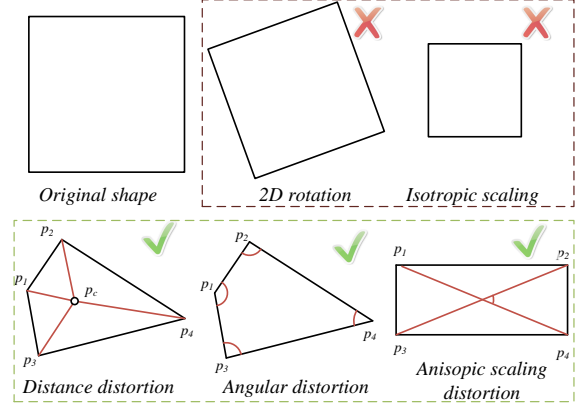


Figure 3: Distortion categories. We measure the distortion degrees except similarity transformation.

our desired decomposition coefficients C_{dec} . Then C_{dec} is input into the homography decomposition module with the predicted homography, which will be decomposed into two bidirectional transformations.

With C_{dec} updating, the motion representations will be updated accordingly, which formulates an iterative process. We set $C_{dec} = \{0, 0, 0, 0\}$ for the first iteration.

Minimal Semantic Distortion To ensure the stitched image contains minimal semantic distortion, we define the distortion distribution map (DDM) and semantic distribution map (SDM). For the distortion distribution, we hold that a similarity transformation would not produce content distortion, including 2D rotation and isotropic scaling, as shown in Fig. 3(top). To measure the deformation caused by non-similarity transformation, we define three types of distortion scores for each vertex, as shown in Fig. 3(bottom). The first type is the **distance distortion score**, which can be calculated as follows:

$$s_i^{distance} = \frac{|\overrightarrow{p_i p_c}|}{\min\{|\overrightarrow{p_i p_c}|\} |i = 1, 2, 3, 4\}} - 1, \quad (8)$$

where p_i represents the vertex and p_c is the center of four vertexes. The second type is the **angular distortion score**, as measured below by the cosine distance:

$$s_1^{angle} = \frac{|\overrightarrow{p_1 p_2} \cdot \overrightarrow{p_1 p_3}|}{|\overrightarrow{p_1 p_2}| \cdot |\overrightarrow{p_1 p_3}|}. \quad (9)$$

Here we calculate p_1 ’s score with its neighboring points as an example; the same regulation goes well for other vertexes. The third type is the **global distortion score**, which is used to describe the magnitude of anisotropic scaling:

$$s^{global} = \frac{|\overrightarrow{p_1 p_4} \cdot \overrightarrow{p_2 p_3}|}{|\overrightarrow{p_1 p_4}| \cdot |\overrightarrow{p_2 p_3}|}, \quad (10)$$

where $\overrightarrow{p_1 p_4}$ and $\overrightarrow{p_2 p_3}$ are diagonals. The **final distortion score** is concluded by associating the three types of distortions as follows:

$$s_i^{final} = s_i^{distance} + s_i^{angle} + s^{global}. \quad (11)$$

With each vertex being assigned a distortion score as Eq. 11, we can grid-sample pixel-wise distortion distribution maps (D_{ref} , D_{tgt}) for each view by bilinear interpolation.

For semantic distribution, we leverage a pretrained VGG19 as the semantic feature extractor. Using the extracted feature maps, we compute the maximum and minimum values across two views, then apply min-max normalization to generate semantic distribution maps (S_{ref} , S_{tgt}).

By aligning DDM and SDM with the same resolution, we define the **semantic distortion loss** for our coefficient generator as:

$$\mathcal{L}_{coef} = \|D_{ref} \cdot S_{ref}\|_1 + \|D_{tgt} \cdot S_{tgt}\|_1. \quad (12)$$

For the iterative process, D_{ref} and D_{tgt} varies as C_{dec} updates. So we encourage all iterations to carry out the constraint of minimal semantic distortion (*i.e.*, Eq. 12) and set an exponentially decaying ratio to balance the significance of each iteration.

Actually, the introduction of \mathcal{L}_{coef} will inevitably degrade the warping performance. To handle this conflict, we propose a **two-stage training scheme**. For the first stage, we train the warping model with each decomposition coefficient being an independent random value between 0 and 1. After the warping model is enabled with the capability to align images with arbitrary coefficients, we freeze this part of parameters and only optimize the coefficient generator.

4 Experiment

4.1 Dataset and Implementation Detail

Detail We implemented our entire model using PyTorch and conducted all experiments on a single RTX 4090Ti GPU. The model training process is divided into two stages: the dual-branch registration network and the iterative coefficient generator. For specific hyperparameter settings, please refer to the supplementary material.

Dataset The datasets used in our experiments consist of two main parts: the UDIS-D dataset and a collection of classic image stitching datasets. The UDIS-D dataset contains 10,440 pairs of training samples and 1,106 pairs of testing samples. The classic image stitching dataset comprises 147 pairs of images across a variety of scenes, primarily sourced from (Lin et al. 2015; Chang, Sato, and Chuang 2014; Chen and Chuang 2016; Li et al. 2017; Herrmann et al. 2018). A detailed description of the collected classic stitching dataset can be found in the supplementary materials.

4.2 Evaluation Metric

Prior works (Nie et al. 2023, 2025; Mei et al. 2024) typically adopt PSNR and SSIM as the evaluation metrics. However, these metrics are computed across the entire image, including invalid pixels after warping, which causes the objective measurements to be biased by the size of invalid regions. Considering that, we adopt masked SSIM and masked PSNR (denoted as mSSIM and mPSNR) as quantitative metrics, which means we compute the average SSIM and PSNR values only for the valid overlapping pixels. Please refer to the supplementary for the specific calculation process.

4.3 Comparative Experiment

To comprehensively evaluate the stitching performance of the proposed algorithm, we conduct a comparative analysis involving 7 stitching algorithms. These include 3 traditional stitching algorithms based on local mesh warping: APAP (Zaragoza et al. 2013), SPW (Liao and Li 2019), and LPC (Jia et al. 2021); 2 learning-based stitching algorithms leveraging global homography: UDIS (Nie et al. 2021b) and DunHuangStitch (Mei et al. 2024); and 2 learning-based stitching algorithms employing TPS warping: UDIS++ (Nie et al. 2023) and StabStitch++ (Nie et al. 2025). StabStitch++ is a video stitching framework, in which the spatial warp is adopted to carry out comparisons with the same number of control points as ours. To visualize the alignment performance, all algorithms adopt average fusion for fairness.

Quantitative Comparison Table 1 and 2 respectively present the alignment performance of various stitching algorithms on the UDIS-D dataset and classical stitching datasets. As shown in Table 1, among traditional stitching algorithms, APAP demonstrates better alignment performance. This is primarily because SPW and LPC impose more constraints to enhance content fidelity, which in turn weakens their alignment capabilities. UDIS and DunHuangStitch, both trained on 128-resolution images and employing a three-stage cascaded global alignment strategy, perform significantly worse than local mesh warping-based algorithms like UDIS++ and StabStitch++, especially on the scenes of parallax.

From Table 2, it can be observed that, due to the robust prior knowledge of feature point detection, traditional stitching algorithms exhibit clear advantages in cross-scene stitching compared to learning-based algorithms. This highlights a critical limitation of learning-based stitching algorithms: their significant cross-scene restrictions and weak generalization capabilities. However, as shown in row 8, the proposed algorithm demonstrates remarkable cross-scene generalization performance, with its zero-shot capability clearly surpassing other learning-based stitching algorithms.

Although the zero-shot performance of the proposed algorithm still lags behind traditional stitching algorithms, we can further enhance its alignment performance using the iterative adaptation strategy proposed in UDIS++. This result indicates that the proposed algorithm not only possesses robust zero-shot cross-scene generalization capabilities but also exhibits stable data-fitting potential.

Qualitative Comparison Here, we only demonstrate the visualization results on classic datasets, with a special highlight on the robustness and naturalness. As illustrated in Fig. 9, LPC algorithm exhibits significant content stretching issues, while UDIS++ tends to produce more background gaps and partial content misalignment. Both of them get abundant invalid pixels because both of them adopt the single-view warp to align images. StabStitch++ employs an intermediate plane and achieves relatively natural stitching results. But its performance on cross-dataset scenes, especially the alignment capability, is not totally satisfactory. In contrast, the proposed algorithm strikes a balance between content alignment and the naturalness of the stitched results, exhibiting

Table 1: Quantitative comparison on the UDIS-D dataset.

Methods		mPSNR \uparrow				mSSIM \uparrow			
		Easy	Moderate	Hard	Average	Easy	Moderate	Hard	Average
1	APAP (Zaragoza et al. 2013)	26.77	22.88	18.75	22.39	0.868	0.770	0.587	0.726
2	SPW (Liao and Li 2019)	25.82	21.49	15.85	20.52	0.844	0.693	0.434	0.634
3	LPC (Jia et al. 2021)	25.01	21.27	17.34	20.82	0.815	0.673	0.485	0.640
4	UDIS (Nie et al. 2021b)	23.53	19.73	17.42	19.94	0.761	0.545	0.376	0.542
5	UDIS++ (Nie et al. 2023)	27.58	23.75	20.04	23.41	0.880	0.792	0.632	0.755
6	DunHuangStitch (Mei et al. 2024)	27.19	23.05	19.10	22.61	0.875	0.767	0.564	0.718
7	StabStitch++ (Nie et al. 2025)	29.92	24.93	20.46	24.63	0.927	0.845	0.664	0.797
8	Ours	29.93	24.96	20.60	24.70	0.926	0.845	0.672	0.800

Table 2: Quantitative comparison on classical datasets. * denotes post processing with the iterative adaptation (Nie et al. 2023).

Methods		mPSNR \uparrow				mSSIM \uparrow			
		Easy	Moderate	Hard	Average	Easy	Moderate	Hard	Average
1	APAP (Zaragoza et al. 2013)	24.33	19.48	14.47	18.92	0.818	0.687	0.442	0.628
2	SPW (Liao and Li 2019)	23.83	19.16	14.66	18.75	0.793	0.647	0.445	0.610
3	LPC (Jia et al. 2021)	23.19	18.67	13.90	18.11	0.761	0.600	0.412	0.573
4	UDIS (Nie et al. 2021b)	20.58	16.27	13.37	16.40	0.660	0.471	0.271	0.454
5	UDIS++ (Nie et al. 2023)	21.93	17.53	13.83	17.36	0.709	0.526	0.325	0.500
6	DunHuangStitch (Mei et al. 2024)	22.02	17.44	13.65	17.29	0.712	0.534	0.319	0.501
7	StabStitch++ (Nie et al. 2025)	23.01	18.08	13.98	17.91	0.751	0.577	0.339	0.534
8	Ours	23.40	18.54	14.67	18.44	0.772	0.607	0.387	0.568
9	Ours*	25.40	19.79	15.48	19.74	0.839	0.691	0.465	0.645

neither obvious content stretching nor excessive background gaps. Our superior visual quality is attributed not only to the use of a dual-branch backbone, which introduces universal prior knowledge and enhances the network’s cross-domain generalization ability, but also to the incorporation of the optimal plane, which ensures the stitching naturalness.

4.4 Ablation Study

Impact of Backbone Table 3 presents the content alignment results obtained using different backbone architectures and whether the proposed dual-branch backbone is employed. The alignment performance on the UDIS-D dataset reflects the algorithm’s generalization ability in similar scenarios, while the performance on classic datasets demonstrates its generalization across different scenarios. Comparing row 1 with row 2, we can observe that a single trainable branch demonstrates superior performance in scenarios with small domain gaps (*i.e.*, UDIS-D), while a single frozen branch excels in large domain gap situations (*i.e.*, classic datasets). We can further notice that the proposed dual-branch architecture integrates both of their advantages, when comparing row 1 and 2 with row 3. Besides, the performance can be further improved using our ternary search strategy, by analysing row 3 and row 4. In addition to ResNet18, we also tried other backbones (*e.g.*, ResNet50), row 5 to 8 reveal the same pattern, which exhibits the universality of our architecture. Finally, we conduct more experiments with each branch adopting different backbones. As shown in row 9 and 10, we replace the frozen branch in row 3 with other backbones, such as ResNet50, and DINOv2-s (Oquab et al. 2023). The results demonstrate that leveraging the same net-

Table 3: Ablation studies on different backbones. All algorithms used $\sigma = 0.5$ for backbone fusion during the inference stage, except \dagger , which used the ternary search strategy to adaptively search for σ .

Backbone		mSSIM \uparrow	
f_{frozen}	f_{train}	UDIS-D	Classic
1	- ResNet18	0.800	0.525
2	ResNet18 -	0.781	0.530
3	ResNet18 ResNet18	0.793	0.543
4	ResNet18 \dagger ResNet18 \dagger	0.800	0.568
5	- ResNet50	0.804	0.519
6	ResNet50 -	0.780	0.529
7	ResNet50 ResNet50	0.799	0.542
8	ResNet50 \dagger ResNet50 \dagger	0.804	0.565
9	ResNet50 ResNet18	0.795	0.535
10	DINOv2-s ResNet18	0.786	0.523

work architectures for the two branches is conducive to constructing unified representations between the activated and frozen branches, yielding better stitching quality.

Impact of Aggregation Strategy Table 4 evaluates the impact of different aggregation strategies (*i.e.*, aggregation position and mode) on the model’s generalization ability. We carry out the evaluation on the classic datasets without ternary search. From that, we can observe two insights. (1) Comparing row 1 and 2 with row 5 shows that integrating information at the feature dimension is less effective for cross-scenario generalization than integrating infor-

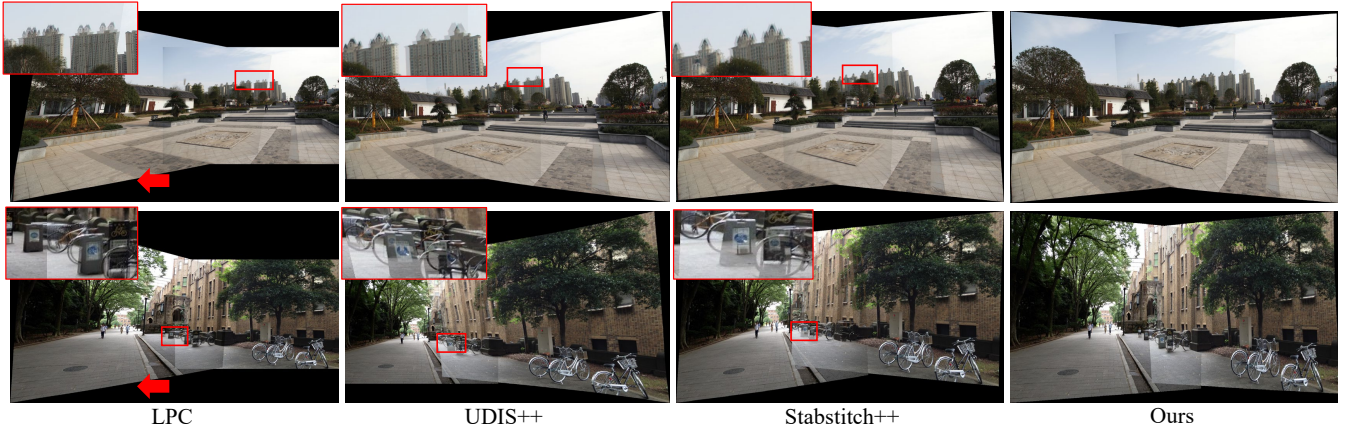


Figure 4: Performance comparison on classical datasets. Arrows indicate regions with noticeable stretching, while rectangular boxes highlight areas with significant content misalignment.

Table 4: Ablation studies using different aggregation strategies during the training stage.

	Aggregation Strategy		mSSIM \uparrow	
	Position	Mode	UDIS-D	Classic
1	Feature ($F^{1/16}$)	Random	0.797	0.537
2	Feature ($F^{1/16}, F^{1/8}$)	Random	0.795	0.536
3	Correlation	Average	0.793	0.525
4	Correlation	Learnable	0.791	0.534
5	Correlation	Random	0.793	0.543

Table 5: The quantitative impact of optimal plane on the alignment and naturalness.

Plane	mSSIM \uparrow		$L_{coef}\downarrow$	
	UDIS-D	Classic	UDIS-D	Classic
1 Refence	0.786	0.537	0.48	0.79
2 Middle	0.800	0.569	0.26	0.49
3 Optimal(ours)	0.800	0.568	0.23	0.42

mation on the correlation level. (2) Comparing row 3 and 4 with row 5 demonstrates that employing a random σ strategy during training can significantly enhance the model’s cross-scenario generalization performance, effectively preventing the frozen and activated backbones from learning homogeneous feature representations.

Impact of Optimal Plane Fig. 5 illustrates the differences between our optimal plane and other planes used for warping. It can be observed that aligning content using either the reference plane or the target plane results in obvious perspective distortions and substantial background invalid regions. As the stitching plane is gradually adjusted, the invalid area is gradually reduced, and distortion is accordingly relieved. Compared with these artificially controlled planes, the optimal plane is optimized with minimal semantic distortions, which preserve the semantically salient regions from unnatural deformation. It is not the plane with the least invalid areas, but the virtual plane with the least

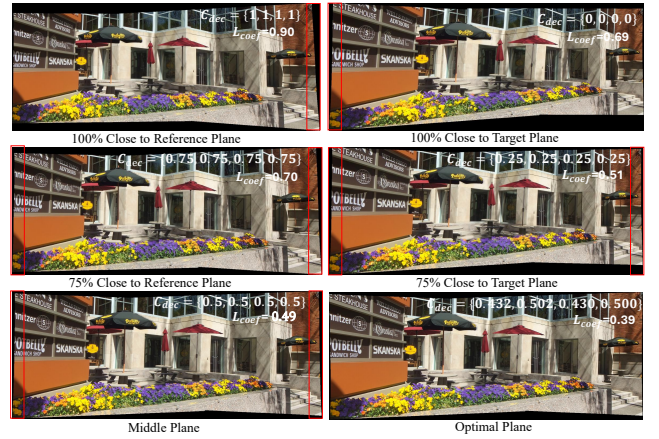


Figure 5: Comparison of stitching results based on different virtual planes.

visually perceptual distortion. Moreover, as shown in Table 6, transitioning the stitching plane from the reference plane to the intermediate plane and finally to our optimal plane improves naturalness (measured by L_{coef}) without compromising alignment performance (quantified by mSSIM). This mutually beneficial outcome is achieved through our carefully designed two-stage training scheme.

5 Conclusion

In this paper, we propose *RopStitch*, a robust and natural image stitching framework. It distinguishes itself from existing solutions through two major contributions. First, it introduces the universal prior of content perception through a dual-branch architecture. This architecture simultaneously aggregates semantically invariant features and fine-grained discriminative features, facilitating cross-domain generalization performance. Then, we present to stitch images on a virtual optimal plane to reduce structure distortions. It redistributes the warping burdens of respective views at the

principle of minimal semantic distortion without sacrificing alignment performance. Experiments across diverse datasets exhibit our superiority over existing methods and validate the universality of its components.

References

- Bookstein, F. L. 1989. Principal warps: Thin-plate splines and the decomposition of deformations. *IEEE TPAMI*, 11(6): 567–585.
- Brown, M.; and Lowe, D. G. 2007. Automatic panoramic image stitching using invariant features. *IJCV*, 74(1): 59–73.
- Cai, S.; Wu, Z.; Guo, L.; Wang, J.; Zhang, S.; Yan, J.; and Shen, S. 2025. Fast and interpretable 2d homography decomposition: Similarity-kernel-similarity and affine-core-affine transformations. *IEEE TPAMI*.
- Cai, W.; and Yang, W. 2025. Object-level geometric structure preserving for natural image stitching. In *AAAI*, volume 39, 1926–1934.
- Chang, C.-H.; Sato, Y.; and Chuang, Y.-Y. 2014. Shape-preserving half-projective warps for image stitching. In *CVPR*, 3254–3261.
- Chen, Y.-S.; and Chuang, Y.-Y. 2016. Natural image stitching with the global similarity prior. In *ECCV*, 186–201.
- Dai, Q.; Fang, F.; Li, J.; Zhang, G.; and Zhou, A. 2021. Edge-guided composition network for image stitching. *Pattern Recognition*, 118: 108019.
- Deng, J.; Dong, W.; Socher, R.; Li, L.-J.; Li, K.; and Fei-Fei, L. 2009. Imagenet: A large-scale hierarchical image database. In *CVPR*, 248–255.
- DeTone, D.; Malisiewicz, T.; and Rabinovich, A. 2016. Deep image homography estimation. *arXiv preprint arXiv:1606.03798*.
- Du, P.; Ning, J.; Cui, J.; Huang, S.; Wang, X.; and Wang, J. 2022. Geometric Structure Preserving Warp for Natural Image Stitching. In *CVPR*, 3688–3696.
- Edstedt, J.; Sun, Q.; Bökman, G.; Wadenbäck, M.; and Felsberg, M. 2024. RoMa: Robust dense feature matching. In *CVPR*, 19790–19800.
- Herrmann, C.; Wang, C.; Bowen, R. S.; Keyder, E.; and Zabih, R. 2018. Object-centered image stitching. In *ECCV*, 821–835.
- Jia, Q.; Feng, X.; Liu, Y.; Fan, X.; and Latecki, L. J. 2023. Learning pixel-wise alignment for unsupervised image stitching. In *ACM MM*, 1392–1400.
- Jia, Q.; Li, Z.; Fan, X.; Zhao, H.; Teng, S.; Ye, X.; and Latecki, L. J. 2021. Leveraging line-point consistence to preserve structures for wide parallax image stitching. In *CVPR*, 12186–12195.
- Jiang, Z.; Zhang, Z.; Fan, X.; and Liu, R. 2022. Towards all weather and unobstructed multi-spectral image stitching: Algorithm and benchmark. In *ACM MM*, 3783–3791.
- Jiang, Z.; Zhang, Z.; Liu, J.; Fan, X.; and Liu, R. 2024. Multispectral image stitching via global-aware quadrature pyramid regression. *IEEE TIP*.
- Kingma, D. P.; Welling, M.; et al. 2013. Auto-encoding variational bayes.
- Kweon, H.; Kim, H.; Kang, Y.; Yoon, Y.; Jeong, W.; and Yoon, K.-J. 2023. Pixel-wise warping for deep image stitching. In *AAAI*, volume 37, 1196–1204.
- Lee, K.-Y.; and Sim, J.-Y. 2020. Warping residual based image stitching for large parallax. In *CVPR*, 8198–8206.
- Li, A.; Guo, J.; and Guo, Y. 2021. Image Stitching Based on Semantic Planar Region Consensus. *IEEE TIP*, 30: 5545–5558.
- Li, J.; Deng, B.; Tang, R.; Wang, Z.; and Yan, Y. 2019. Local-adaptive image alignment based on triangular facet approximation. *IEEE TIP*, 29: 2356–2369.
- Li, J.; Wang, Z.; Lai, S.; Zhai, Y.; and Zhang, M. 2017. Parallax-tolerant image stitching based on robust elastic warping. *IEEE TMM*, 20(7): 1672–1687.
- Li, Z.; Lv, X.; Yu, W.; Liu, Q.; Lin, J.; and Zhang, S. 2024. Face shape transfer via semantic warping. *Visual Intelligence*, 2(1): 26.
- Liao, T.; and Li, N. 2019. Single-perspective warps in natural image stitching. *IEEE TIP*, 29: 724–735.
- Liao, T.; and Li, N. 2022. Natural Image Stitching Using Depth Maps. *arXiv preprint arXiv:2202.06276*.
- Liao, T.; Wang, C.; Li, L.; Liu, G.; and Li, N. 2025. Parallax-tolerant image stitching via segmentation-guided multi-homography warping. *Signal Processing*, 230: 109860.
- Lin, C.-C.; Pankanti, S. U.; Natesan Ramamurthy, K.; and Aravkin, A. Y. 2015. Adaptive as-natural-as-possible image stitching. In *CVPR*, 1155–1163.
- Lowe, D. G. 2004. Distinctive image features from scale-invariant keypoints. *IJCV*, 60: 91–110.
- Ma, S.; Gao, J.; Wang, R.; Chang, J.; Mao, Q.; Huang, Z.; and Jia, C. 2023. Overview of intelligent video coding: from model-based to learning-based approaches. *Visual Intelligence*, 1(1): 15.
- Mei, Y.; Yang, L.; Wang, M.; Yu, T.; and Wu, K. 2024. DunHuangStitch: Unsupervised Deep Image Stitching of Dunhuang Murals. *IEEE TVCG*.
- Nie, L.; Lin, C.; Liao, K.; Liu, M.; and Zhao, Y. 2020. A view-free image stitching network based on global homography. *Journal of Visual Communication and Image Representation*, 73: 102950.
- Nie, L.; Lin, C.; Liao, K.; Liu, S.; and Zhao, Y. 2021a. Depth-aware multi-grid deep homography estimation with contextual correlation. *IEEE TCSVT*, 32(7): 4460–4472.
- Nie, L.; Lin, C.; Liao, K.; Liu, S.; and Zhao, Y. 2021b. Unsupervised deep image stitching: Reconstructing stitched features to images. *IEEE TIP*, 30: 6184–6197.
- Nie, L.; Lin, C.; Liao, K.; Liu, S.; and Zhao, Y. 2023. Parallax-Tolerant Unsupervised Deep Image Stitching. In *ICCV*, 7399–7408.
- Nie, L.; Lin, C.; Liao, K.; Zhang, Y.; Liu, S.; and Zhao, Y. 2025. StabStitch++: Unsupervised Online Video Stitching with Spatiotemporal Bidirectional Warps. *IEEE TPAMI*.

- Nie, L.; Lin, C.; Liao, K.; and Zhao, Y. 2022. Learning edge-preserved image stitching from multi-scale deep homography. *Neurocomputing*, 491: 533–543.
- Oquab, M.; Darcet, T.; Moutakanni, T.; Vo, H.; Szafraniec, M.; Khalidov, V.; Fernandez, P.; Haziza, D.; Massa, F.; El-Nouby, A.; et al. 2023. Dinov2: Learning robust visual features without supervision. *arXiv preprint arXiv:2304.07193*.
- Song, D.-Y.; Lee, G.; Lee, H.; Um, G.-M.; and Cho, D. 2022. Weakly-Supervised Stitching Network for Real-World Panoramic Image Generation. In *ECCV*, 54–71. Springer.
- Von Gioi, R. G.; Jakubowicz, J.; Morel, J.-M.; and Randall, G. 2008. LSD: A fast line segment detector with a false detection control. *IEEE TPAMI*, 32(4): 722–732.
- Zaragoza, J.; Chin, T.-J.; Brown, M. S.; and Suter, D. 2013. As-projective-as-possible image stitching with moving DLT. In *CVPR*, 2339–2346.
- Zhang, Y.; Lai, Y.; Lang, N.; Zhang, F.-L.; and Xu, L. 2024. RecStitchNet: Learning to stitch images with rectangular boundaries. *Computational Visual Media*.

A Loss Function

The complete loss function used for model training is shown as follows:

$$\mathcal{L} = \mathcal{L}_{align} + w_s \mathcal{L}_{shape} + w_c \mathcal{L}_{coef}, \quad (13)$$

where \mathcal{L}_{align} and \mathcal{L}_{shape} constrain content alignment and shape preservation, respectively. \mathcal{L}_{coef} represents the optimal plane constraint that has been carefully discussed in the manuscript. w_s and w_c are the corresponding weights, which are set to 4 and 10.

A.1 Content Alignment Term

The content alignment term can be divided into two parts: global alignment using homography and local alignment using TPS. The specific formulas are as follows:

$$\begin{aligned} \mathcal{L}_{align} &= \mathcal{L}_{align}^H + w \mathcal{L}_{align}^{TPS}, \quad \text{where} \\ \mathcal{L}_{align}^H &= \lambda \|I_{ref} \cdot \psi(\mathcal{I}, \mathcal{H}) - \psi(I_{tgt}, \mathcal{H})\|_1 \\ &\quad + \lambda \|I_{tgt} \cdot \psi(\mathcal{I}, \mathcal{H}^{-1}) - \psi(I_{ref}, \mathcal{H}^{-1})\|_1, \\ \mathcal{L}_{align}^{TPS} &= w_{tps} \cdot \psi(\mathcal{I}, \mathcal{TPS}) - \psi(I_{ref}, \mathcal{TPS})\|_1. \end{aligned} \quad (14)$$

λ and w_{tps} are the balancing weights, which are set to 0.5 and 4.

A.2 Shape Term

The shape term includes an intra-grid constraint and an inter-grid constraint as:

$$\mathcal{L}_{shape} = \mathcal{L}_{shape}^{intra} + \mathcal{L}_{shape}^{inter}. \quad (15)$$

This allows for a reasonable magnitude of image warping and ensures consistent motions of neighboring control points. Denoting the resolution of input images as $H \times W$, we define the TPS control points evenly distributed on the whole image with $(U + 1) \times (V + 1)$ points. These control points can be regarded as the vertices of a $U \times V$ mesh.

Intra-grid Constraint To prevent excessive deformation of the mesh, we set a minimum length and width in both horizontal and vertical directions. This constraint restricts the generated mesh from being too small and causing dramatic scaling. Denoting \vec{i} and \vec{j} as the unit vectors in the horizontal and vertical directions, we can formulate this constraint as:

$$\begin{aligned} \mathcal{L}_{shape}^{intra} &= \frac{1}{(U+1) \times V} \sum L_h^{intra} + \frac{1}{U \times (V+1)} \sum L_v^{intra}, \\ \text{where } \mathcal{L}_h^{intra} &= RELU(\alpha \frac{W}{V} - |\langle \vec{e}_h, \vec{i} \rangle|), \\ \mathcal{L}_v^{intra} &= RELU(\alpha \frac{H}{U} - |\langle \vec{e}_v, \vec{j} \rangle|). \end{aligned} \quad (16)$$

L_h^{intra} and L_v^{intra} represent the intra-grid constraint terms in the horizontal and vertical directions, respectively. \vec{e}_h and \vec{e}_v represent the direction vectors connected by neighboring points in the horizontal and vertical directions, respectively. α is set to 1/8, and both U and V are set to 12.

Inter-grid Constraint To prevent straight structures from bending, the neighboring grids should undergo similar transformations. Given consecutive edges $e_{t_1}^{\vec{e}}$ and $e_{t_2}^{\vec{e}}$ in two neighboring grids, the inter-grid loss can be expressed as follows:

$$\mathcal{L}_{shape}^{inter} = \frac{1}{K} \sum (1 - \frac{\langle e_{t_1}^{\vec{e}}, e_{t_2}^{\vec{e}} \rangle}{\|e_{t_1}^{\vec{e}}\| \cdot \|e_{t_2}^{\vec{e}}\|}), \quad (17)$$

where K denotes the number of tuples of two consecutive edges in the mesh.

B More Experiment Detail

B.1 Detail

We implemented our entire model using PyTorch and conducted all experiments on a single RTX 4090Ti GPU. The model training process includes two stages: the dual-branch registration network and the iterative coefficient generation network.

In the first stage, we only train the dual-branch alignment network. During this phase, the iterative coefficient generation network is not involved in the training process. Instead, both the σ and C_{dec} parameters are randomly initialized to values between 0 and 1 for each batch. This strategy enhances the model's ability to learn robust features, which is similar to the use of μ and σ in Variational Autoencoders (VAE) (Kingma, Welling et al. 2013). For optimization, we use the AdamW optimizer with an initial learning rate of $4 \times e^{-5}$, and apply an exponential decay schedule to dynamically adjust the learning rate in each epoch. The model is trained for a total of 100 epochs.

In the second stage, we freeze the parameters of the dual-branch alignment network and only train the iterative coefficient generation network with σ set to 0.5. Additionally, unlike the first stage, we use the Adam optimizer with an initial learning rate of $1 \times e^{-4}$ to train for another 50 epochs.

B.2 Dataset

The experiments were conducted using the UDIS-D (Nie et al. 2021b) dataset and another dataset composed of classic image stitching examples. The latter was specifically constructed to comprehensively evaluate the robustness of the algorithm and consists of 147 pairs of classic traditional image stitching matches, covering a wide variety of stitching scenarios. Some examples from this dataset are shown in Fig. 6, including scenes with varying parallax, moving objects, significant illumination differences, and images with different aspect ratios. With these diverse representative samples, we could assess the algorithm's adaptability and robustness in complex real-world environments.

B.3 Evaluation Metric

We adopt mSSIM and mPSNR (masked SSIM and masked PSNR) in quantitative experiments, which are defined as:

$$\begin{aligned} mSSIM &= \frac{\sum_{p \in I} M_{olp}(p) \cdot SSIM(p)}{\sum_{p \in I} M_{olp}(p)}, \\ mPSNR &= 20 \times \log_{10}(\frac{1}{mRMSE(I)}). \end{aligned} \quad (18)$$

Here, $mRSME$ denotes the RMSE over the overlapping area, while M_{olp} is a mask to identify the overlapping region, as previously described in the paper. The SSIM is computed using a window size of 7.

C More Comparative Result

Stitching Quality in Various Scenes Fig. 7 and 8 present additional stitching results of various algorithms on the UDIS-D dataset as well as on classic traditional datasets.

Zero-Shot Results of Learning-based Solutions Fig. 9 shows the zero-shot performance of various learning-based stitching algorithms on cross-domain datasets. The results indicate that the proposed algorithm exhibits superior scene generalization ability over existing learning-based solutions.

Inference Time Table 6 presents the stitching speeds of various algorithms at different resolutions. Since traditional stitching algorithms cannot leverage GPU acceleration, we only report their inference speeds on the CPU. In contrast, the speed of learning-based stitching algorithms is measured with a single RTX 4090Ti GPU. As the results show, the inference time of traditional algorithms is significantly slower than that of learning-based methods, and this gap becomes more pronounced as the image resolution increases. Additionally, while the proposed algorithm is slightly slower than other deep learning-based methods at lower resolutions, the difference in speed diminishes as the resolution increases.

Table 6: Comparisons on inference time (/s). These methods are tested with ¹ Intel(R) Xeon(R) Silver 4314 CPU @ 2.40GHz. and ² NVIDIA RTX 4090 GPU.

Dataset	Railtrack	Tower	Carpark
Resolution	2000 × 1500	1280 × 960	490 × 653
APAP ¹	20.921	4.455	2.005
SPW ¹	227.762	29.390	6.583
LPC ¹	2805.300	130.047	40.443
UDIS++ ²	0.416	0.139	0.092
DunHuangStitch ²	0.930	0.466	0.206
StabStitch++ ²	0.511	0.201	0.102
Ours ²	0.647	0.326	0.227

D More Ablation Study.

Impact of Search Strategy Table 7 presents the content alignment results on classic stitching datasets using both the fixed threshold search strategy and the dynamic ternary search strategy proposed in this paper. It can be observed that searching within the interval $[-1, 2]$ yields significantly better results than searching within $[0, 1]$.

This demonstrates the complementary nature of the frozen feature representations to the activated feature representations, further confirming that the dual-branch backbone can effectively enhance the model’s cross-scenario generalization performance. In addition, comparing the fixed threshold search strategy with the dynamic ternary search strategy reveals that the latter possesses a stronger local search

capability. Finally, considering computational efficiency, we ultimately adopted 10 dynamic ternary search iterations.

Table 7: Ablation studies on search strategies in the testing stage. The experiments are conducted on classic datasets.

Search Strategy			Classic	
	Threshold	Step	Range	mPSNR↑ mSSIM↑
1	Fixed	5	$[-1, 2]$	18.36 0.561
2	Fixed	5	$[0, 1]$	18.30 0.556
3	Fixed	10	$[-1, 2]$	18.45 0.567
4	Fixed	10	$[0, 1]$	18.31 0.559
5	Fixed	20	$[-1, 2]$	18.45 0.568
6	Fixed	20	$[0, 1]$	18.33 0.560
7	Dynamic	10	$[-1, 2]$	18.48 0.568
8	Dynamic	20	$[-1, 2]$	18.49 0.571

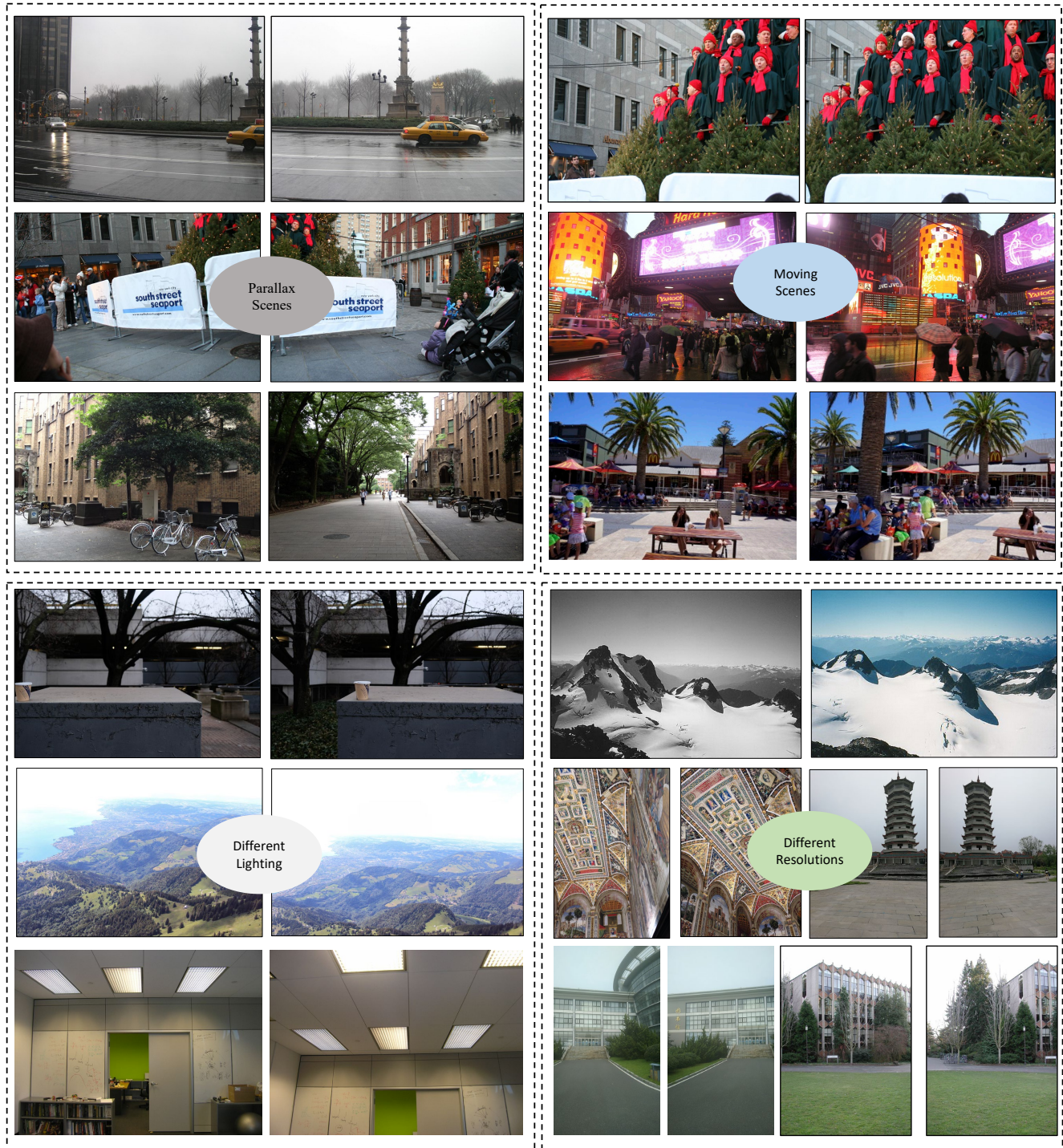


Figure 6: Examples of classic image stitching dataset.

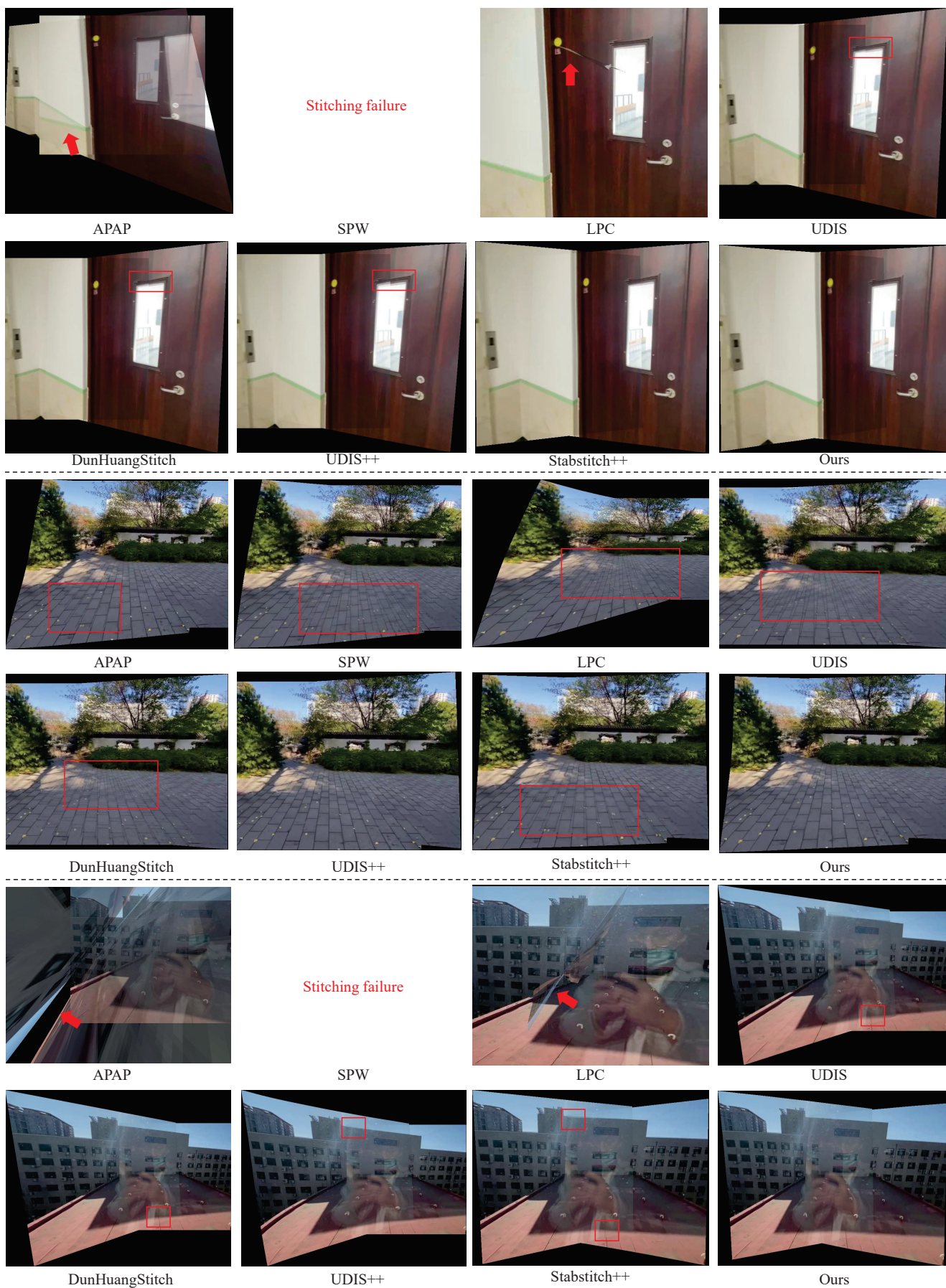


Figure 7: Performance comparison on the UDIS-D dataset. Arrows indicate regions with noticeable stretching, while rectangular boxes highlight areas with significant content misalignment.

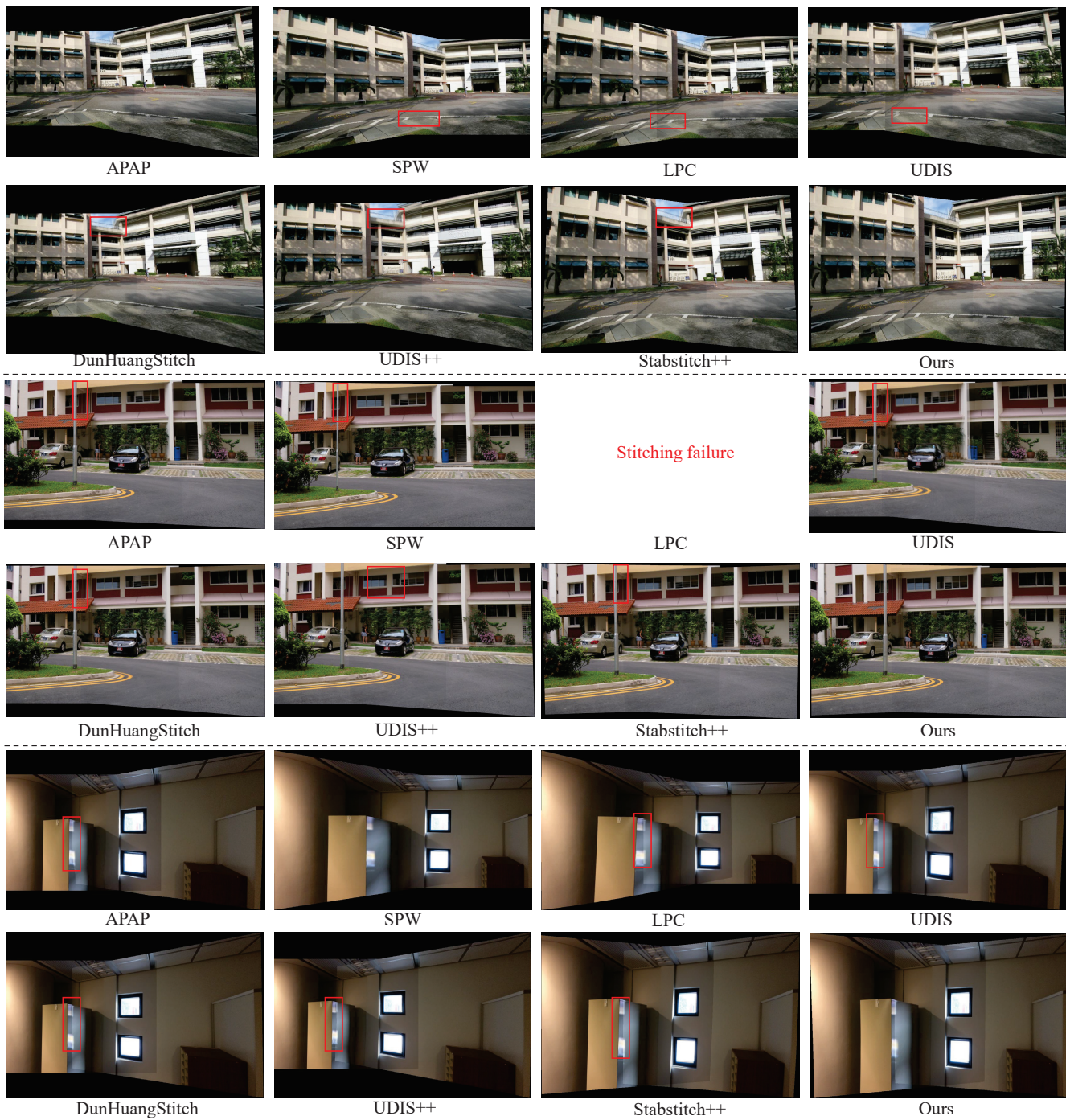


Figure 8: Performance comparison on classical datasets. Arrows indicate regions with noticeable stretching, while rectangular boxes highlight areas with significant content misalignment.

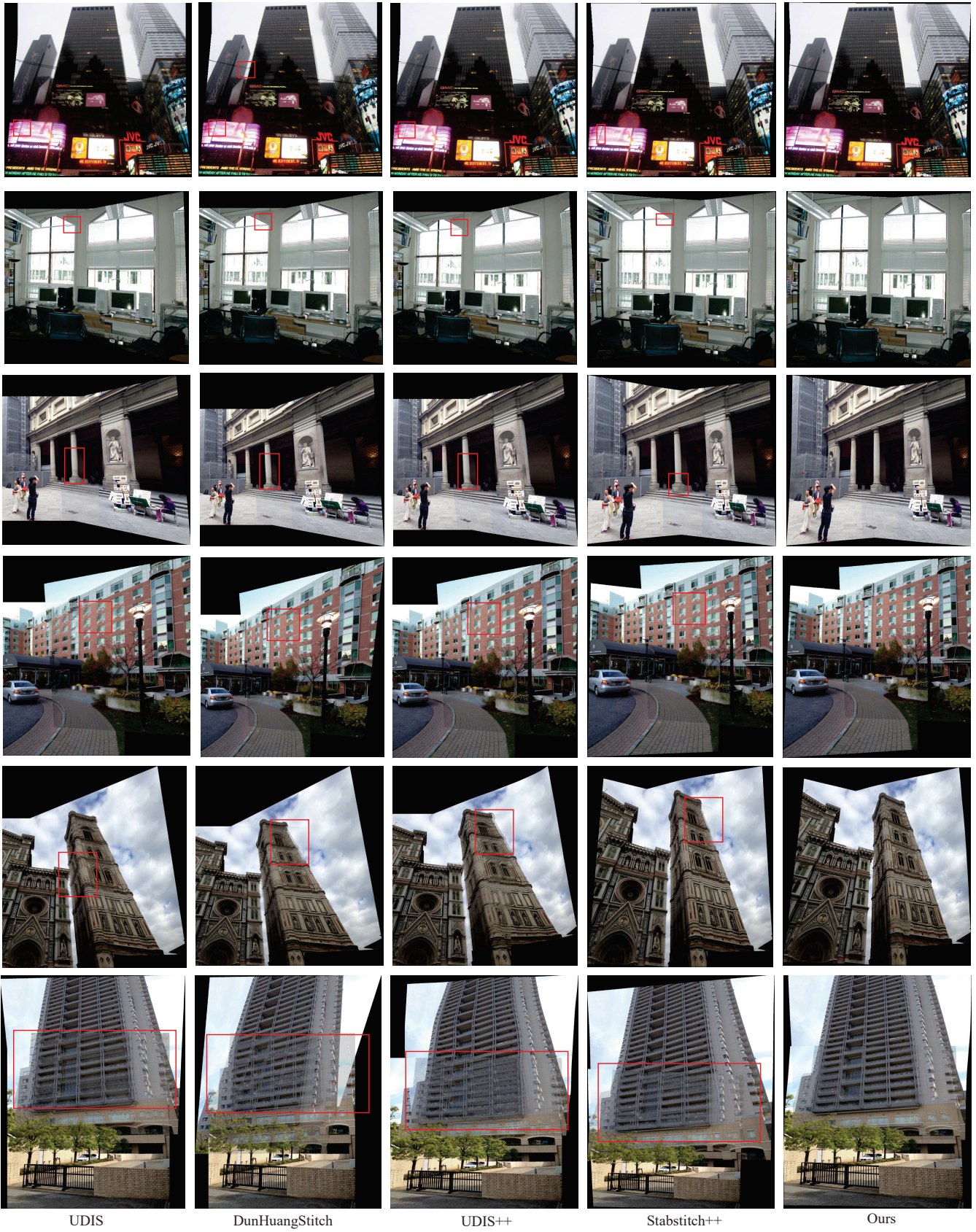


Figure 9: Zero-shot comparative results of learning-based stitching algorithms.